Influence of interface layer insertion on the spin Seebeck effect and the spin Hall magnetoresistance of $Y_3Fe_5O_{12}$/Pt bilayer systems

Takumi Niimura,[1] Yuichiro Kurokawa,[1] Shu Horiike,[1] Houlin Li,[1] Hiroki Hanamoto,[1]
Ramon Weber ,[2] Andreas Berger ,[2] and Hiromi Yuasa[1]

[1]*Faculty of Information Science and Electrical Engineering, Kyushu University, Fukuoka 819-0395, Japan*
[2]*CIC nanoGUNE BRTA, E-20018 Donostia-San Sebastian, Spain*

We observe significantly enhanced spin Seebeck effect (SSE) and spin Hall magnetoresistance (SMR) values by inserting 0.3–0.6-nm-thick layers of magnetic materials with different composition (Cr, $Ni_{80}Fe_{20}$, $Co_{90}Fe_{10}$, $Fe_{50}Co_{50}$, and Fe) at the $Y_3Fe_5O_{12}$/Pt interface. To study the actual magnetic state of these insertion layers, we, then, investigated the magnetization of these layers via generalized magneto-optical ellipsometry. Magnetic insertion layers in this thickness range did not exhibit a measurable magnetization, even though our method should have detected even a small fraction of the bulk magnetization value for the utilized materials easily. Therefore, the observed SSE and SMR enhancement generated by the insertion of thin magnetic material layers did not result from a net interface magnetization but might, instead, be related to the paramagnetic state of the inserted layers.

I. INTRODUCTION

Spin current manipulation has attracted increasing attention both in application and fundamental research fields because of its zero Joule heating properties. A typical phenomenon is the spin Seebeck effect (SSE), which is the spin current propagation driven by a temperature gradient in a magnetic layer [1–11]. The attachment of a heavy-metal layer onto a magnetic layer results in spin pumping, which is dependent on the spin mixing conductance at their interface [12–18]. The resulting spin current is converted into electric current by the inverse spin Hall effect (ISHE) in the heavy-metal layer, which can then be utilized for novel thermoelectric devices having wide applicability, e.g., as energy harvesters, heat flow sensors, and two-dimensional thermal mapping sensors [5,19,20]. Given the Onsager reciprocal relation with ISHE, the spin Hall effect (SHE) also occurs in the heavy-metal layer, meaning that the electric current is converted back into a spin current [20–23]. Based on the SHE, the spin Hall magnetoresistance (SMR) is observed in such bilayers consisting of magnetic insulator and heavy-metal layers; also this SMR strongly depends on the spin mixing conductance and the spin Seebeck power generation [18,24–27]. Therefore, to use the spin current for either SSE or SMR applications, it is paramount that the spin mixing conductance will be further improved. This parameter is significantly determined by the interface quality [28–30] and, according to a theoretical study, also by the magnetic moment density at the magnetic insulator/heavy-metal interface [31]. In a previous work [32], we experimentally increased the SSE voltage by inserting a $Ni_{80}Fe_{20}$ layer in between $Y_3Fe_5O_{12}$ (YIG) and Pt and, thus, observed agreement with this theoretical prediction. Here, let us mention that we confirmed that there is merely negligible moment in Pt for all samples with and without

insertion layers by x-ray magnetic circular dichroism (XMCD) at the BL39XU of SPring-8.

In this paper, we systematically investigated both the SSE and SMR of YIG/Pt devices by inserting thin layers of magnetic materials with different saturated magnetization and composition, namely, Cr, $Ni_{80}Fe_{20}$, $Co_{90}Fe_{10}$, $Fe_{50}Co_{50}$, and Fe. We also analyzed the magnetic properties of these layers via generalized magneto-optical ellipsometry (GME) measurements and determined their correlation with the spin pumping in SSE and SMR.

II. EXPERIMENTAL

Figure 1 illustrates the sample structure and the SSE, SMR, and GME measurement systems. We prepared two types of samples: one with a sintered YIG substrate (1-mm thick) and the other with a sputtered YIG film (50-nm thick) for the SSE voltage, and the SMR and GME measurements, respectively. The 50-nm YIG film was deposited on a thermally oxidized Si substrate via radiofrequency magnetron sputtering and, then, annealed in atmosphere at $750\,^{\circ}$C for 1 h. The M (t-nm)/Pt (5-nm) films (M = Cr, $Ni_{80}Fe_{20}$, $Co_{90}Fe_{10}$, $Fe_{50}Co_{50}$, or Fe; t = thickness from 0 to 1.0 nm) were deposited onto the YIG film or substrate.

The crystal structure of the sintered and sputtered YIG layers was investigated via cross-sectional transmission electron microscopy (TEM) and high-angle annular dark-field scanning TEM (HAADF-STEM) observations on milled samples by using an H-9000NAR microscope (Hitachi Hitech) operated at 300 kV and a JEM-ARM200F system (Nihon Denshi) operated at 200 kV, respectively. Additionally, they were characterized by x-ray diffraction (XRD) using a Rigaku SmartLab system. The electromotive force related to the
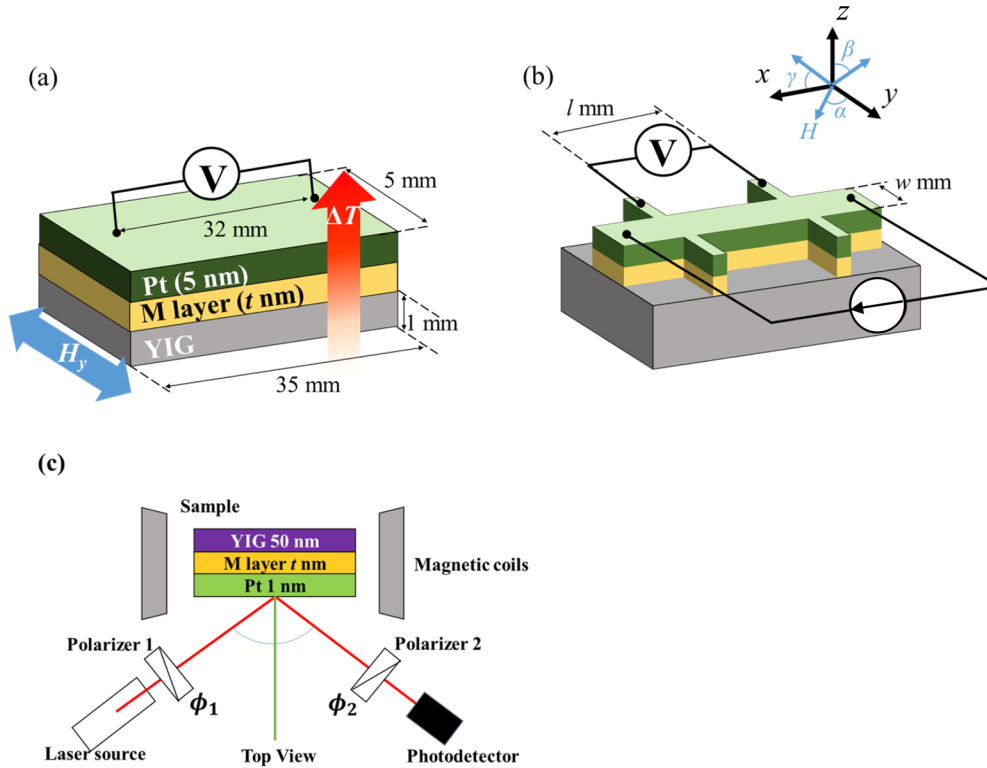
FIG. 1. Schematics of the sample structure along with the (a) thermoelectric voltage, (b) resistance change, and (c) GME measurement systems. In the measurement of MR_{xx} dependence on H, a current was passed along the x-axis direction, and the external magnetic-field (H) changed in the y-axis direction. For the measurement of MR_{xx} dependence on α, β, and γ, a current was passed along the x-axis direction, and a constant H was rotated on the xy plane, the yz plane, and the xz plane, respectively. In the GME measurements, two polarizers (P1 and P2) were mounted on stages and rotated by the angles ϕ_1 and ϕ_2, respectively.

SSE was measured within a temperature gradient applied by sandwiching the samples in between a pair of Peltier modules in a thermal bath; specifically, we monitored the temperature difference (ΔT) between the top and the bottom of the sample as shown in Fig. 1(a). ΔT was measured at the Peltier module surface, within 1 mm from the sample surface so that the monitored ΔT could be slightly larger than the actual temperature discrepancy of the sample surfaces. It is noted that, even if there is an error in the measured ΔT, it will be virtually identical for all samples, given that the same setup is used and given the very similar nature of all samples and their thermal conductivity. The magnetic field was swept from -300 to $+300$ mT, and the generated voltage (ΔV) was detected by two probes separated by a distance (l) of 32 mm. Thus, based on ΔV, the spin Seebeck coefficient (S) was calculated as $S = \Delta V\, t_{YIG}/\Delta T\, l$, where t_{YIG} is the thickness of the sintered YIG substrate (i.e., 1 mm) [32,33].

The magnetoresistance associated with SMR was evaluated by means of a four-terminal measurement method as shown in Fig. 1(b). The upper M/Pt layers were patterned into stripes with a width (w) of 10 mm and length (l) of 20 mm. The MR_{xx}-H_y curves were obtained by varying the external field (H_y) from -150 to 150 mT; the MR_{xx}-α, MR_{xx}-β, and MR_{xx}-γ curves were measured by changing the angles (α, β, and γ) between external field and charge current from $0°$ to $360°$ at a fixed field magnitude of 123 mT. For the MR_{xx}-H_y

curves, $\Delta R_{xx} = R_{max} - R_{min}$ and $MR_{xx} = \Delta R_{xx}/R_{max}$. For the $MR_{xx} - \alpha$, β, and γ curves, $\Delta R_{xx} = R(90°) - R(45°)$ and $MR_{xx} = \Delta R_{xx}/R(45°)$.

The inserted magnetic material layers were much thinner than the YIG ones, hindering their magnetization measurement via typical methods, such as vibrating sample magnetometry (VSM) or by using superconducting quantum interference devices (SQUIDs). Therefore, we utilized a magneto-optical technique, specifically the GME method to investigate the magnetization states and values of the inserted film because this method is surface sensitive and, moreover, enables one to tune the sample depth at which the method reaches its highest sensitivity [34–39]. GME is a light reflection technique using a sequential set of incoming light polarizations and detection sensitivity settings to evaluate the entire reflection matrix in an absolute quantitative manner, which is the maximum information achievable by any optical experiment with polarization degree conservation. Thus, it allows for very precise sample to sample comparisons. The sample structure and GME measurement setup are schematically shown in Fig. 1(c). The samples, consisting of a Pt layer with a thickness of 1 nm instead of 5 nm and a sputtered YIG film, were prepared so as to emphasize the optical signals from the inserted magnetic material layers. In our GME measurements, we monitor the light intensity (I) whereas changing H and obtaining hysteresis loops for a certain number of settings of the polarizer orientation (ϕ_1, ϕ_2) where ϕ_1 and ϕ_2 are the
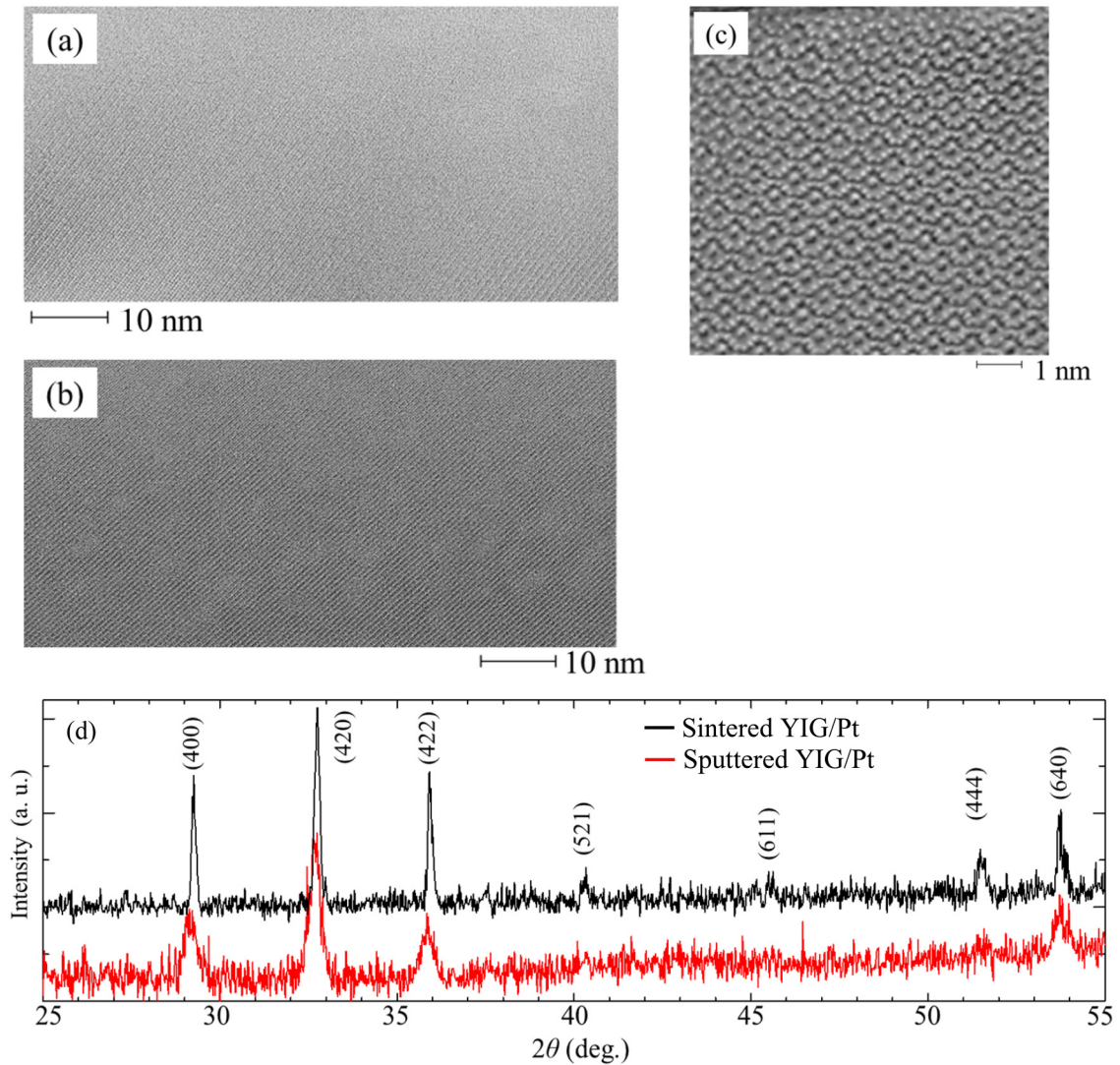
FIG. 2. Cross-sectional TEM images ($\times 2\,000\,000$ magnification) of the (a) sintered YIG substrate and the (b) sputtered YIG film on SiO$_2$ substrate. (c) High-angle annular dark-field scanning TEM image of the sputtered YIG film ($\times 20\,000\,000$ magnification). (d) θ-2θ XRD pattern for a sintered YIG substrate and grazing incidence x-ray diffraction (GXRD) pattern for a sputtered YIG film on SiO$_2$.

polarizer angles with respect to the plane of incidence in the incident and reflected light paths, respectively. From these original hysteresis loop data, we derived the magnetically induced relative light intensity variation (dI/I), where dI is the light intensity change due to the magnetic state inversion as a function of ϕ_1, ϕ_2 at every applied field value of H. The magnetic-field H was swept from -130 to $+130$ mT. Further details about the GME technique can be found elsewhere [36]. The SMR and GME measurements were all performed at a room temperature.

III. RESULTS AND DISCUSSION

Figures 2(a) and 2(b) show the cross-sectional TEM images of the sintered and the sputtered YIG substrates, revealing a fine-crystalline structure in both cases. Since the grain size was larger than one field view of the microscope (75 nm), the grain boundaries could not be observed. To clarify the YIG

atomic order, we analyzed the sputtered sample via HAADF-STEM analysis [Fig. 2(c)], finding a well-oriented crystalline structure, sufficient for the spin pumping experiments. Figure 2(d) shows a θ-2θ XRD pattern for a sintered YIG substrate and GXRD pattern for a sputtered YIG film on SiO$_2$. The typical YIG diffraction peaks were observed in both measurements, which means YIG has a single garnet structure phase [40].

Before discussing the SSE and SMR, let us first consider phenomena that might overlap with them, namely, the anomalous Nernst effect (ANE) and anisotropic magnetoresistance (AMR) in the inserted magnetic material layers. First, the resulting electromotive voltage includes both the ANE and the SSE voltages because the ANE generates an electromotive force in the direction perpendicular to the temperature gradient and the magnetic field, which is the same direction as for the SSE voltage. Thus, to quantitatively investigate the ANE contribution to the total electromotive voltage, we fabricated a
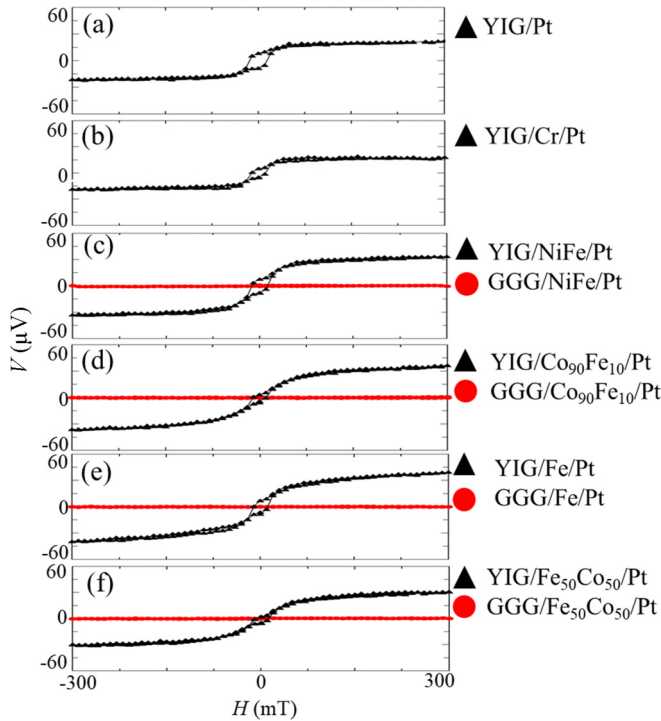
FIG. 3. Thermoelectric V-H curves at a temperature difference sputtered of 15 K for the YIG/M (1-nm)/Pt (5-nm) and $Gd_3Ga_5O_{12}$ (GGG)/M (1-nm)/Pt (5-nm) samples, where M denotes (a) none, (b) Cr, (c) $Ni_{80}Fe_{20}$, (d) $Co_{90}Fe_{10}$, (e) Fe, and (f) $Fe_{50}Co_{50}$.

set of reference samples by using $Gd_3Ga_5O_{12}$ (GGG), instead, of YIG as the substrate, which do not allow SSE voltage observation. Figures 3(a)–3(f) shows the V-H curves for the YIG/M (1-nm)/Pt (5-nm) and GGG/M (1-nm)/Pt (5-nm) samples when applying a temperature difference of 15 K between their top and bottom sides, revealing a much lower voltage for the GGG substrate samples. See the Supplemental Material in Ref. [41] of V-H (Fig. S1) for YIG/M (t nm)/Pt (5 nm) where M denotes Cr, $Ni_{80}Fe_{20}$, $Co_{90}Fe_{10}$, $Fe_{50}Co_{50}$, Fe, or no M layer and t is 0, 0.3, 0.6, and 1.0 nm. The two-step

behavior is due to the shape anisotropy of YIG in Fig. S1 of the Supplemental Material [41].

This finding indicates that the ANE contribution to the total electromotive force was negligible compared with the SSE voltage. All samples containing magnetic layers of different compositions and thicknesses exhibited similar results, that is, all the GGG/M/Pt samples showed far lower voltages than the corresponding YIG/M/Pt ones. Therefore, we can conclude that the ANE contribution in our YIG samples is negligible and, thus, the electromotive force is mainly generated by SSE.

Here, let us compare the V-H curves for samples with the sintered and sputtered YIG. Figure 4(a) shows the V-H curves at an effective temperature difference of 15 K for the sintered or sputtered YIG/Pt (5-nm) sample. The variation of V for both samples are in good agreement, suggesting that the two types of YIG have comparable surface states and quantily regarding spin injection. However, the shapes of V-H curves are different. As far as the sintered YIG substrate is used, a two-step behavior was observed in all V-H curves, whereas, it was absent when sputtered YIG was used. It was confirmed by XRD data in Fig. 2(d) that no other crystalline phase but the garnet structure can be detected, but there remains a possibility of different magnetic phases. To investigate the reason of this inconsistency between sintered and sputtered YIG samples, we compared the V-H and M-H curves for the sintered YIG/Pt (5-nm) samples in Fig. 4(b). It was found that the M-H curve does not exhibit the two-step behavior unlike the V-H curve, which was previously reported and explained by the suppression of SSE in the low magnetic field derived from the magnon scattering near domain walls in Ref. [3].The difference between the sintered and the sputtered YIG is not only their texture, but also the thickness. Since it was confirmed that both YIG sample types have a highly oriented crystalline structure by cross-sectional TEM observation, we considered the thickness as the main reason for the occurrence or absence of the two-step characteristic. This is consistent with reports that the V-H curve shape gradually changes, and the two-step characteristic appears upon increasing the thickness of YIG [5]. Therefore, it is
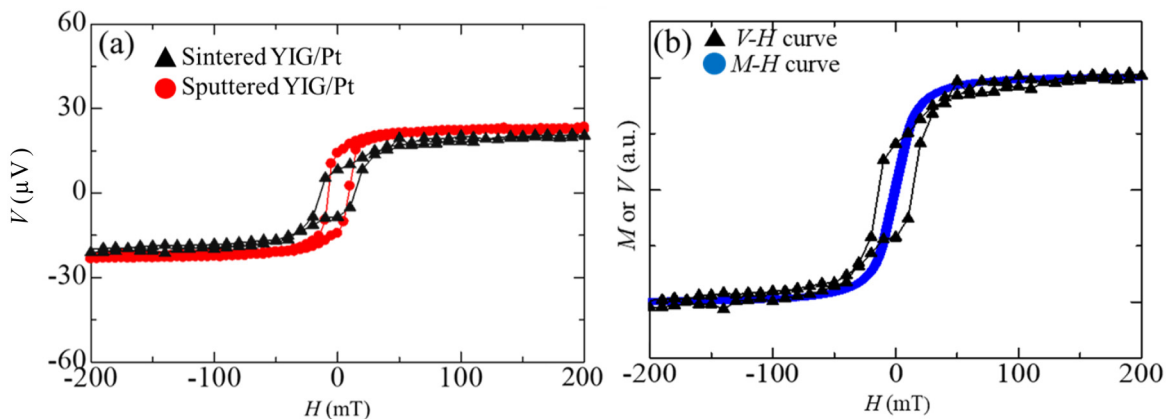

FIG. 4. (a) Thermoelectric V-H curves at a temperature difference of 15 K for sintered or sputtered YIG/Pt(5-nm) samples. A good agreement for the magnitude of voltage change was observed. (b) Magnetization curve and V-H curve at a temperature difference of 15 K for the sintered YIG/Pt (5-nm) sample. A two-step characteristic was observed in the V-H curve but not in the M-H curve.
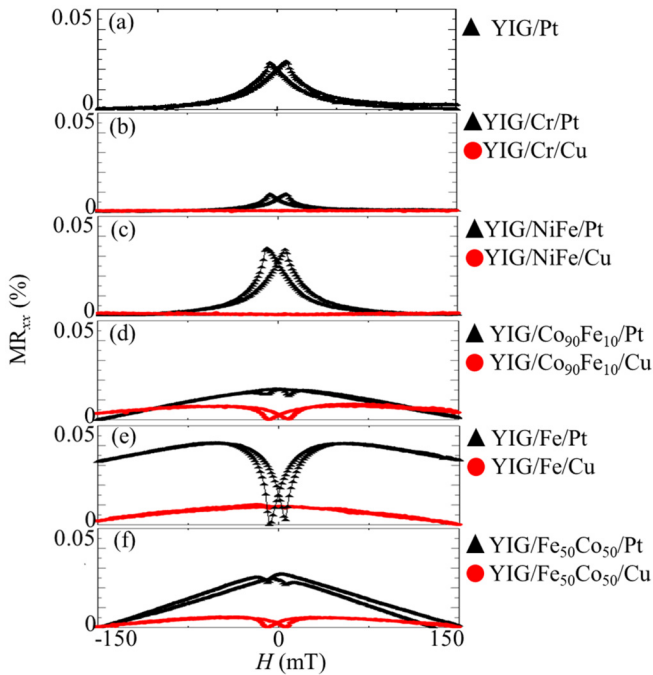
FIG. 5. MR_{xx}-Hy curves for the various YIG/M (1-nm)/Pt (5-nm) and YIG/M (1-nm)/Cu (5-nm) samples, where M denotes (a) none, (b) Cr, (c) $Ni_{80}Fe_{20}$, (d) $Co_{90}Fe_{10}$, (e) Fe, and (f) $Fe_{50}Co_{50}$.

supposed that the thick YIG had the different magnetic domains from the one found in thin YIG and SSE is suppressed in low magnetic fields, which causes the two-step in the V-H curve.

Next, we investigated the AMR contribution to the total magnetoresistance by fabricating another reference sample set by using Cu instead of Pt. Since Cu exhibits only a small spin Hall angle resulting in small SHE, SMR was hardly detected in the YIG/Cu samples, unlike for the YIG/Pt ones [24,42]. Figures 5(a)–5(f) displays the MR_{xx}-H_y curves for our YIG/M (1-nm)/Cu (5-nm) and YIG/M(1-nm)/Pt (5-nm) samples, where M denotes Cr, $Ni_{80}Fe_{20}$, $Co_{90}Fe_{10}$, $Fe_{50}Co_{50}$, and Fe, as well as the absence of the interface layer M for comparison. See the Supplemental Material in Ref. [41] for the MR_{xx}-H_y curves for YIG/M (t nm)/Pt (5 nm) where M denotes Cr, $Ni_{80}Fe_{20}$, $Co_{90}Fe_{10}$, $Fe_{50}Co_{50}$, and Fe and t is 0, 0.3, 0.6, and 1.0 nm in Fig. S2 of the Supplemental Material [41]. When M was Cr or $Ni_{80}Fe_{20}$, the magnetoresistance ratio MR_{xx} of the YIG/M/Cu samples was much smaller than that of the YIG/M/Pt ones, which means that the AMR in Cr or $Ni_{80}Fe_{20}$ was negligible compared to the SMR in the YIG/M/Pt samples. However, we observed different results when M was $Co_{90}Fe_{10}$, $Fe_{50}Co_{50}$, or Fe. In this case, it was difficult to completely ignore the MR_{xx} of YIG/M/Cu against that of YIG/M/Pt; in other words, when the M thickness was 1 nm, the AMR in the magnetic insertion layer overlapped with the SMR in YIG/M/Pt. Moreover, the AMR effect in magnetic layers can be further enhanced by an adjacent Pt film [43]. YIG/($Co_{90}Fe_{10}$, $Fe_{50}Co_{50}$, or Fe)/Pt samples exhibited larger MR_{xx} effects than the YIG/($Co_{90}Fe_{10}$, $Fe_{50}Co_{50}$, or Fe)/Cu structures, but due to fact that even the AMR alone might be enhanced by the adjacent Pt film, we could not exactly

estimate the SMR by simply computing the difference MR_{xx} (YIG/M/Pt) $-$ MR_{xx} (YIG/M/Cu) for our samples with M thicknesses of 1 nm. We also measured MR_{xx}-α curves for all our samples since it is difficult to align R_{xx} and H_y exactly perpendicular in the MR_{xx}-H_y measurement setup. Additionally, it is difficult to separate SMR and AMR perfectly as long as the magnetic field is applied in plane so that we also measured MR_{xx}-β and γ curves for some our samples. In the following discussion, the MR_{xx} values derived from these MR_{xx}-α curves are used given their better accuracy. Figure 6 shows results of SMR measurements whereas rotating angles α, β, or γ for our YIG/M (0.3, 0.6, 1-nm)/Pt (5-nm) samples with M being Cr, $Ni_{80}Fe_{20}$, $Co_{90}Fe_{10}$, Fe, or $Fe_{50}Co_{50}$, as well as for a sample without M being present. All these measurements were performed in an external field of 0.6 T. These experimental results clearly indicate that the AMR contribution to MR_{xx} was negligible compared with the SMR as long as the M thickness is only 0.3 nm. On the other hand, when the M thickness is 0.6 or 1.0 nm, we need to survey our data carefully. At a M thickness of 1 nm for $Co_{90}Fe_{10}$, Fe, and $Fe_{50}Co_{50}$, our samples exhibit AMR and its contribution to MR_{xx} is not negligible, which makes these samples' utility for the present study very limited. This observation is related to the fact that a thickness of approximately 1 nm should be the critical thickness at which a stable magnetization at room temperature emerges for these materials. When the insertion layer thickness is 0.6 nm, Fe and $Fe_{50}Co_{50}$ show a small AMR contribution in MR_{xx}-γ and their magnitude ratio to MR_{xx}-β was estimated to be approximately 7.9% and 12.7%, respectively. Since the AMR contribution is limited but it cannot be ignored, we treat these data separately from other data in the following.

In addition, we observed for M being 1-nm $Co_{90}Fe_{10}$ or 1-nm Fe that the MR_{xx}-β curves are not sine curves but exhibit steep changes around β of 90° and 270°, which means that the magnetization is not saturated perpendicular to the surface plane. This behavior was observed even after increasing the field to 0.9 T. As such curves do not correspond well to these samples' magnetization, we did not plot the MR_{xx}-β curves for them.

Figure 7 shows the experimentally determined S values of the SSE and MR_{xx} values of the SMR as a function of the thickness of the inserted magnetic material layers. The SMR data for $Co_{90}Fe_{10}$, $Fe_{50}Co_{50}$, and Fe layers with thicknesses of 1.0 nm were not plotted because we could not distinguish the AMR contribution in these cases. Also, the SMR data for $Fe_{50}Co_{50}$ and Fe layers with thicknesses of 0.6 nm were plotted as opened circles since they include a small AMR contribution as mentioned above. Both S and MR_{xx} increased significantly upon adding an insertion layer of thickness of 0.3 or 0.6 nm. Compared to this, the corresponding M composition dependencies of these parameters were slightly complicated; S attained its maximum value when inserting Fe and $Co_{90}Fe_{10}$, whereas the MR_{xx} maximum value was observed in the Fe case. To carefully compare the S and MR_{xx} results, Fig. 8 illustrates their relationship for two different M thicknesses (0.3 and 0.6 nm). A clear correlation between the SSE and the SMR results can be observed, that is, samples with higher S exhibit also higher MR_{xx}. Since both SSE and SMR are based on spin pumping that strongly depends on
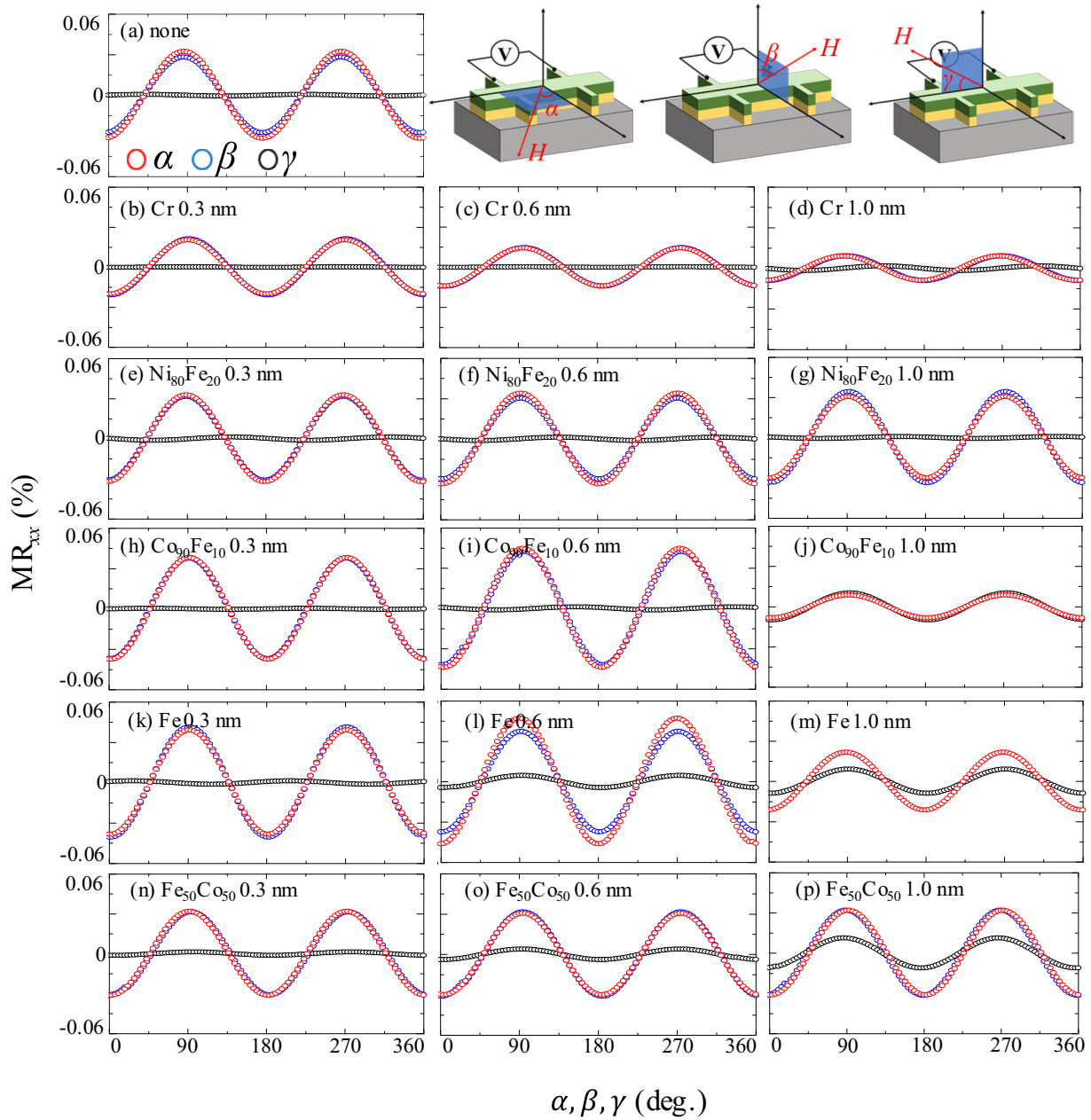
FIG. 6. MR_{xx}-α, MR_{xx}-β, and MR_{xx}-γ curves for YIG/M (0.3 nm, 0.6 nm, 1 nm)/Pt (5 nm) with M being Cr, $Ni_{80}Fe_{20}$, $Co_{90}Fe_{10}$, Fe, and $Fe_{50}Co_{50}$, as well as without M being present.

the spin mixing conductance, this correlation is a reasonable result.

Now, we discuss the magnetization of the inserted M layers since our original strategy was to increase the magnetic moment density at the interface between the magnetic and the heavy-metal layers. Before discussing the measurements themselves, let us consider the saturated magnetization for the bulk state of each material from the Slater-Pauling curve [44,45]. Figure 9 shows the dependencies of S and MR_{xx} on the magnetic moment per atom for each M layer in the Slater-Pauling curve. Except for $Fe_{50}Co_{50}$, both the S and the MR_{xx} values increase with the bulk magnetization value, which is consistent with a previous theoretical report [31].

However, although the $Fe_{50}Co_{50}$ layer exhibited the largest magnetization in the Slater-Pauling curve, both its S and MR_{xx} values were smaller than those of $Ni_{80}Fe_{20}$, $Co_{90}Fe_{10}$, and Fe, in contrast with initial expectations. This might be due to the disagreement between the magnetization of the M layer and the bulk state reported in literature since the magnetic layers are extremely thin (subnanometers). With this in mind, it is crucial to characterize the actual magnetization state of the inserted layers in our samples. However, typical magnetization measurement methods, such as via VSM and SQUID, provide only results averaged over all layers and, thus, cannot determine the magnetization of each layer separately, and given the very small thickness of the insertion layer, its overall
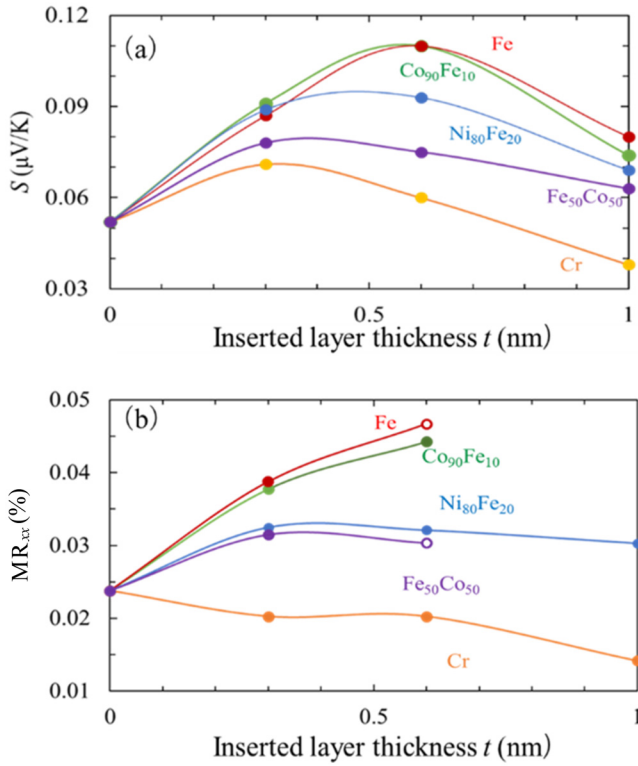
FIG. 7. (a) Spin Seebeck coefficient (S) and (b) magnetoresistance change (MR_{xx}) of the spin Hall magnetoresistance as functions of the thickness of the inserted magnetic layers.
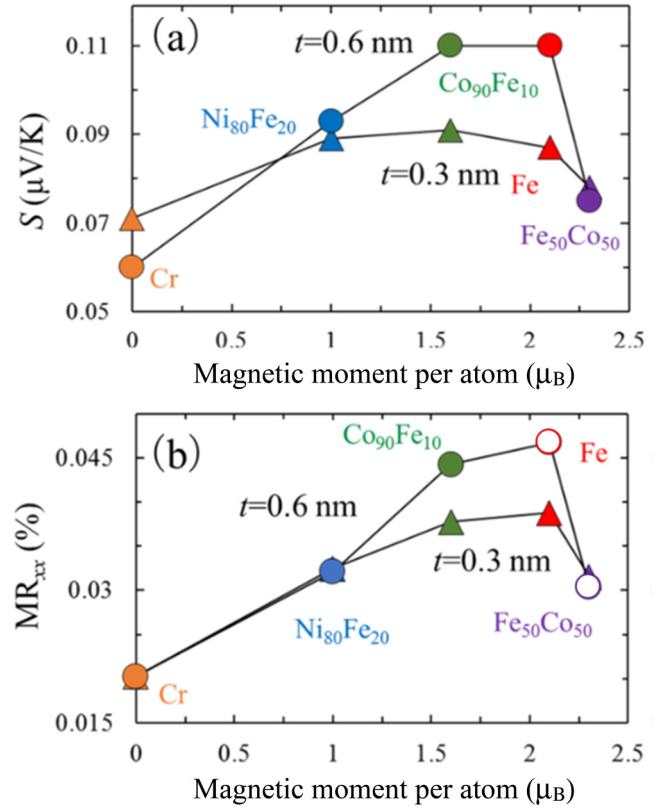

FIG. 8. Relation between the spin Seebeck coefficient (S) in spin Seebeck effect and the magnetoresistance change (MR_{xx}) in the spin Hall magnetoresistance for inserted magnetic layers having different composition and a thickness of (a) 0.3 or (b) 0.6 nm.

FIG. 9. Dependence of the spin Seebeck coefficient (S) and the magnetoresistance change (MR_{xx}) on the magnetic moment per atom; the triangle and circle plots represent the data for magnetic layers having a thickness of 0.3 and 0.6 nm, respectively.

contribution to the total magnetization is too small to be reliably separated; hence, we conducted GME measurements to achieve an enhanced sensitivity to the magnetization of the inserted layer.

As an example of the experimentally obtained GME data, Figs. 10(a)–10(d) illustrates experimental $dI/I(\phi_1, \phi_2)$ maps for our YIG/Pt (1-nm) and YIG/Ni$_{80}$Fe$_{20}$ (0.6-nm)/Pt (1-nm) samples in sufficiently large positive and negative magnetic fields. The normalized light intensity variation under magnetic state inversion was analyzed by utilizing [34]

$$\frac{dI}{I} = 4\frac{B_1 f_1 + B_2 f_2 + B_3 f_3 + B_4 f_4 + B_5 f_5 + B_6 f_6}{I_0 + f_3 + B_7 f_7 + 2B_8 f_4}, \quad (1)$$

where the B_i factors represent the elements of the reflection matrix (in particular, B_1 and B_2 are the coefficients for the longitudinal Kerr effect and, thus, the most relevant magnetization information for our experimental geometry), the $f_i = f_i(\phi_1, \phi_2)$ factors are analytical functions of ϕ_1 and ϕ_2, and I_0 is the background signal. Numerical B_i values were derived from our experimental dI/I maps via least-squares fits of Eq. (1), whose results are shown in Figs. 10(e)–10(h). Most of the coefficients of determination R^2 were higher than 0.96, which guarantees a high accuracy of the B_i factors derived from the fitting. The R^2 value in Fig. 10(e) was only 0.9358, which is still acceptable since it was obviously caused by isolated experimental data scattering at $\phi_1 = 94.5$ and $\phi_2 = -6.5$ in Fig. 10(a).
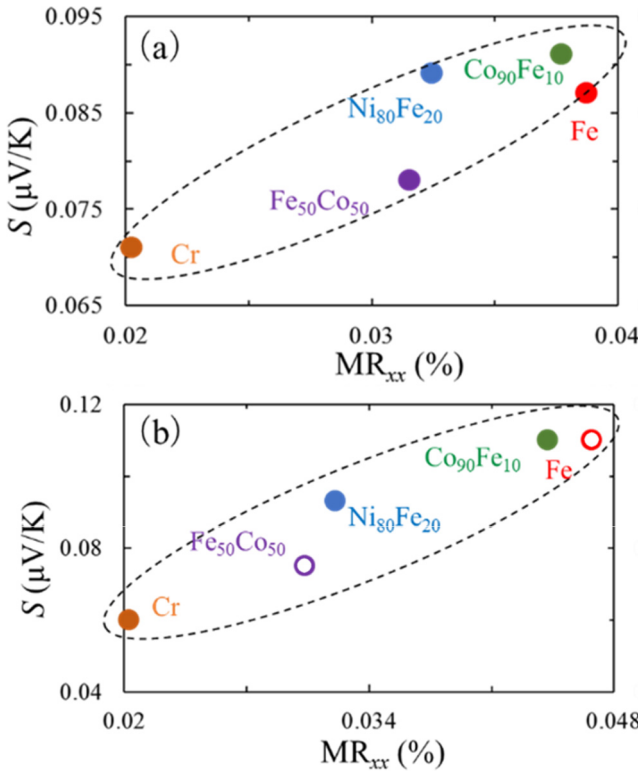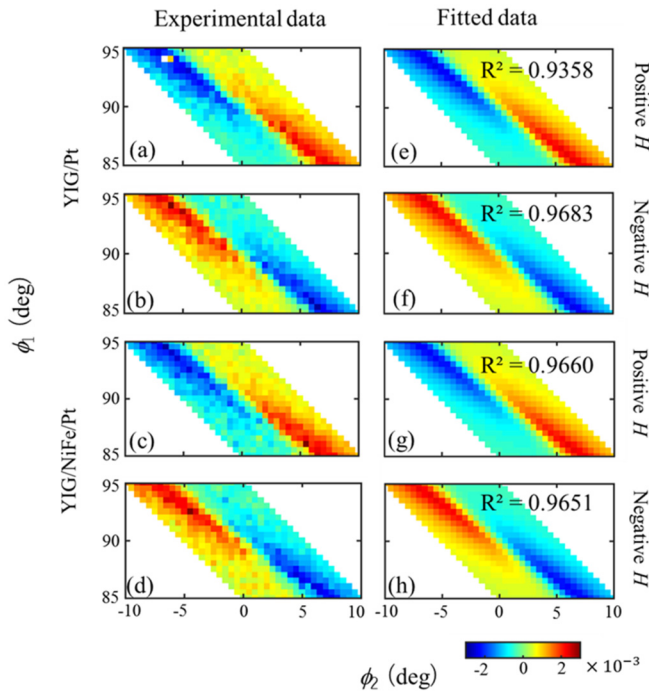
FIG. 10. dI/I maps, that is magnetically induced I variation as a function of ϕ_1, ϕ_2, for the $Y_3Fe_5O_{12}$ (YIG) (50 nm)/Pt (1 nm) (a), (b), (e), and (f) and YIG (50-nm)/$Ni_{80}Fe_{20}$ (0.6-nm)/Pt (1-nm) samples (c), (d), (g), and (h). (a)–(d) display experimental maps, and (e)–(h) display least-squares fits of these experimental maps to Eq. (1).

Since we measured in longitudinal-magneto-optical Kerr effect (MOKE) geometry, we focus here on B_1 and B_2. Figure 11 compares their experimental and simulated values as a function of the magnetic field for the YIG (50-nm)/Pt (1-nm) and YIG (50-nm)/$Ni_{80}Fe_{20}$ (0.6-nm)/Pt (1-nm) samples. In the case of the simple YIG/Pt structure, the simulated and experimental results exhibit very good agreement, suggesting the appropriateness of the simulation conditions and

materials constant utilized. In contrast, the YIG/$Ni_{80}Fe_{20}$/Pt curve simulated when assuming that the inserted $Ni_{80}Fe_{20}$ layer possesses magnetization and a corresponding magneto-optical constant Q (which was measured for a thick $Ni_{80}Fe_{20}$ film) was widely different from the experimental one; on the contrary, when the Q value for $Ni_{80}Fe_{20}$ was artificially set to zero, i.e., a vanishing magnetization assumed whereas using the previously determined optical properties of $Ni_{80}Fe_{20}$, the simulated, and experimental data agreed well. This indicates that the magnetization of the inserted $Ni_{80}Fe_{20}$ layer was close to zero. The data in Fig. 11, furthermore, show that the noise level and point to point variation of our GME data are far smaller than the expected signal change for a ferromagnetic $Ni_{80}Fe_{20}$ layer, highlighting both the ability of GME to measure magnetic responses of thin interface layers and the fact that any existing magnetization in the $Ni_{80}Fe_{20}$ film cannot be more than a few percent of its bulk magnetic moment if it is present at all. All other YIG/M/Pt samples with M thicknesses of 0.3 and 0.6 nm showed the same results as the YIG/$Ni_{80}Fe_{20}$/Pt data shown here, meaning that all the inserted layers with a thickness of 0.3 or 0.6 nm did not possess any relevant magnetization. These experimental results indicate that the thin M layers we used in our sample structures have Curie temperatures lower than room temperature since the Curie temperature of magnetic films decreases with decreasing film thickness [46–48], and the adjacent ferromagnetic YIG layer is not able to stabilize a ferromagnetic state in these ultrathin insertion layers at room temperature unlike in the layers over 1.0 nm. Therefore, we can conclude that it is not a ferromagnetic moment at the YIG/Pt interface that improves the SSE and SMR in our samples.

Let us consider another possible explanation for the SSE and SMR increase by taking into account that the inserted layers of 0.6 nm or thinner did not exhibit a ferromagnetic state. Nonetheless, we do observe that our experimental SSE and SMR values showed a rather significant correlation with the literature magnetic moment of the insertion material as discussed in Fig. 9. In general, the paramagnetic moment per atom can be determined via the Curie-Weiss law of bulk
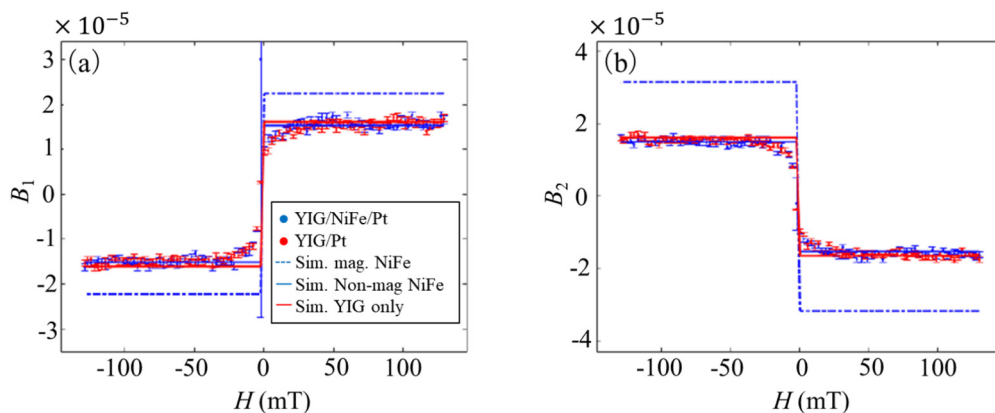

FIG. 11. Magnetic-field (H) dependence of the (a) B_1 and (b) B_2 factors, both representing the longitudinal MOKE. The dots denote the experimental values determined by fitting the acquired dI/I maps of the YIG (50-nm)/$Ni_{80}Fe_{20}$ (0.6-nm)/Pt (1-nm) and YIG (50-nm)/Pt (1-nm) samples at every field value. The blue dashed and solid lines represent the results simulated by assuming that the $Ni_{80}Fe_{20}$ (0.6-nm) layer possessed a bulk like magnetization or none at all, respectively. The red solid line indicates the simulated results for the YIG (50-nm)/Pt (1-nm) sample.

samples at high temperature, and one finds a close correlation in between paramagnetic moment and (anti)ferromagnetic moment through a constant factor for all materials, as long as the band structure does not significantly change at the magnetic phase transition. For instance, Fe in $Ni_{35}Fe_{65}$ has the moment of $1.4\,\mu_B$ and $2.3\,\mu_B$ in paramagnetic and ferromagnetic state, respectively [49]. In a similar fashion, Cr has the moment of $0.28\,\mu_B$ and $0.58\,\mu_B$ in the paramagnetic and antiferromagnetic states, respectively [50]. Thus, the insertion layers are expected to have a paramagnetic moment dependence very similar to the moment of the ordered state, which is a quantity that is typically far easier to access. Thus, it is sensible to assume that our insertion layers build up a locally spin-polarized magnetic state without achieving ferromagnetic order throughout the film at room temperature. Thus, overall, our data suggest that the insertion layers are in a paramagnetic state. Actually, SSE has been already reported in paramagnetic insulators at low temperature and attributed to short-range magnetic interactions [51]. In itinerant magnetic materials, there is a strong correlation between a thermal spin fluctuation and the magnetic susceptibility (χ), according to the SCR theory [52,53]; moreover, the spin mixing conductance is proportional to the momentum sum of the imaginary part of the dynamical transverse susceptibility, $\sum_k \mathrm{Im}\,\chi_k^R$ [54]. Furthermore, the experimental spin pumping enhancement near an order temperature has been explained by spin fluctuations [39,55]. From all of the above considerations, it seems very sensible to conclude that SSE and SMR were improved by spin fluctuation enhancements in the inserted layers, given their paramagnetic nature due to their very small thickness (subnanometers). In thicker insertion layers than 0.6 nm, SSE and SMR are decreased upon increasing the insertion layer thickness to 1.0 nm, which corresponds to the fact that thicker insertion layers with the higher-order temperature restrain spin fluctuation at room temperature.

IV. CONCLUSION

We inserted five different magnetic materials into a YIG/Pt interface and investigated the resulting S of SSE and MR_{xx} of SMR. In each case, we observed enhancement in both SSE and SMR as long as the inserted layer was no thicker than 0.6 nm. The GME analysis revealed that such thin layers did not exhibit a ferromagnetic magnetization, leading to the conclusion that it is not a static magnetic moment at the interface with Pt that was the dominant reason for the spin pumping enhancement; thus, we attributed the main cause of SSE and SMR improvement to spin fluctuation enhancements at the interfaces based upon the lack of static magnetization and the materials trend that we observe in our sample series.

[1] K. Uchida, S. Takahashi, K. Harii, J. Ieda, W. Koshibae, K. Ando, S. Maekawa, and E. Saitoh, Observation of the spin Seebeck effect, Nature (London) **455**, 778 (2008).

[2] K. Uchida, J. Xiao, H. Adachi, J. Ohe, S. Takahashi, J. Ieda, T. Ota, Y. Kajiwara, H. Umezawa, H. Kawai, G. E. W. Bauer, S. Maekawa, and E. Saitoh, Spin Seebeck insulator, Nat. Mater. **9**, 894 (2010).

[3] K. Uchida, H. Adachi, T. Ota, H. Nakayama, S. Maekawa, and E. Saitoh, Observation of longitudinal spin-Seebeck effect in magnetic insulators, Appl. Phys. Lett. **97**, 172505 (2010).

[4] S. Y. Huang, W. G. Wang, S. F. Lee, J. Kwo, and C. L. Chien, Intrinsic Spin-Dependent Thermal Transport, Phys. Rev. Lett. **107**, 216604 (2011).

[5] A. Kirihara, K. Uchida, Y. Kajiwara, M. Ishida, Y. Nakamura, T. Manako, E. Saitoh, and S. Yorozu, Spin-current-driven thermoelectric coating, Nat. Mater. **11**, 686 (2012).

[6] N. Roschewsky, M. Schreier, A. Kamra, F. Schade, K. Ganzhorn, S. Meyer, H. Huebl, S. Geprägs, R. Gross, and S. T. B. Goennenwein, Time resolved spin Seebeck effect experiments, Appl. Phys. Lett. **104**, 202410 (2014).

[7] A. Kirihara, K. Kondo, M. Ishida, K. Ihara, Y. Iwasaki, H. Someya, A. Matsuba, K. Uchida, E. Saitoh, N. Yamamoto, S. Kohmoto, and T. Murakam, Flexible heat-flow sensing sheets based on the longitudinal spin Seebeck effect using one-dimensional spin-current conducting films, Sci. Rep. **6**, 23114 (2016).

[8] K. Uchida, H. Adachi, T. Kikkawa, A. Kirihara, M. Ishida, S. Yorozu, S. Maekawa, and E. Saitoh, Thermoelectric generation based on spin Seebeck effects, Proc. IEEE **104**, 1946 (2016).

[9] A. Sola, P. Bougiatioti, M. Kuepferling, D. Meier, G. Reiss, M. Pasquale, T. Kuschel, and V. Basso, Longitudinal spin Seebeck coefficient: heat flux vs. temperature difference method, Sci. Rep. **7**, 46752 (2017).

[10] J. Cramer, U. Ritzmann, B.-W. Dong, S. Jaiswal, Z. Qiu E. Saitoh, U. Nowak, and M. Kläu, Spin transport across antiferromagnets induced by the spin Seebeck effect, J. Phys. D: Appl. Phys. **51**, 144004 (2018).

[11] E. Y. Vedmedenko, R. K. Kawakami, D. D. Sheka, P. Gambardella, A. Kirilyuk, A. Hirohata, C. Binek, O. Chubykalo-Fesenko, S. Sanvito, B. J. Kirby, J. Grollier, K. Everschor-Sitte, T. Kampfrath, C. Y. You, and A. Berger, The

2020 magnetism roadmap, J. Phys. D: Appl. Phys. **53**, 453001 (2020).

[12] K. Uchida, A. Kirihara, M. Ishida, R. Takahashi, and E. Saitoh, Local spin-Seebeck effect enabling two-dimensional position sensing, Jpn. J. Appl. Phys. **50**, 120211 (2011).

[13] E. Saitoh, M. Ueda, H. Miyajima, and G. Tatara, Conversion of spin current into charge current at room temperature: Inverse spin-Hall effect, Appl. Phys. Lett. **88**, 182509 (2006).

[14] K. Ando, Y. Kajiwara, S. Takahashi, S. Maekawa, K. Takemoto, M. Takatsu, and E. Saitoh, Angular dependence of inverse spin-Hall effect induced by spin pumping investigated in a $Ni_{81}Fe_{19}$/Pt thin film, Phys. Rev. B **78**, 014413 (2008).

[15] Y. Tserkovnyak, A. Brataas, and G. E. W. Bauer, Spin pumping and magnetization dynamics in metallic multilayers, Phys. Rev. B **66**, 224403 (2002).

[16] O. Mosendz, J. E. Pearson, F. Y. Fradin, G. E. W. Bauer, S. D. Bader, and A. Hoffmann, Quantifying Spin Hall Angles from Spin Pumping: Experiments and Theory, Phys. Rev. Lett. **104**, 046601 (2010).

[17] J. Xiao, G. E. W. Bauer, K. Uchida, E. Saitoh, and S. Maekawa, Theory of magnon-driven spin Seebeck effect, Phys. Rev. B **81**, 214418 (2010).

[18] M. Weiler, M. Althammer, M. Schreier, J. Lotze, M. Pernpeintner, S. Meyer, H. Huebl, R. Gross, A. Kamra, J. Xiao, Y. Chen, H. Jiao, G. E. W. Bauer, and S. T. B. Goennenwein, Experimental Test of the Spin Mixing Interface Conductivity Concept, Phys. Rev. Lett. **111**, 176601 (2013).

[19] M. Weiler, M. Althammer, F. D. Czeschka, H. Huebl, M. S. Wagner, M. Opel, I. Imort, G. Reiss, A. Thomas, R. Gross, and S. T. B. Goennenwein, Local Charge and Spin Currents in Magnetothermal Landscapes, Phys. Rev. Lett. **108**, 106602 (2012).

[20] J. E. Hirsch, Spin Hall Effect, Phys. Rev. Lett. **83**, 1834 (1999).

[21] Y. K. Kato, R. C. Myers, A. C. Gossard, and D. D. Awschalom, Observation of the spin Hall effect in semiconductors, Science **306**, 1910 (2004).

[22] J. Wunderlich, B. Kaestner, J. Sinova, and T. Jungwirth, Experimental Observation of the Spin-Hall Effect in a Two-Dimensional Spin-Orbit Coupled Semiconductor System, Phys. Rev. Lett. **94**, 047204 (2005).

[23] S. O. Valenzuela and M. Tinkham, Direct electronic measurement of the spin Hall effect, Nature (London) **442**, 176 (2006).

[24] H. Nakayama, M. Althammer, Y.-T. Chen, K. Uchida, Y. Kajiwara, D. Kikuchi, T. Ohtani, S. Geprägs, M. Opel, S. Takahashi, R. Gross, G. E. W. Bauer, S. T. B. Goennenwein, and E. Saitoh, Spin Hall Magnetoresistance Induced by a Nonequilibrium Proximity Effect, Phys. Rev. Lett. **110**, 206601 (2013).

[25] M. Althammer, S. Meyer, H. Nakayama, M. Schreier, S. Altmannshofer, M. Weiler, H. Huebl, S. Geprägs, M. Opel, R. Gross, D. Meier, C. Klewe, T. Kuschel, J.-M. Schmalhorst, G. Reiss, L. Shen, A. Gupta, Y.-T. Chen, G. E. W. Bauer, E. Saitoh, and S. T. B. Goennenwein, Quantitative study of the spin Hall magnetoresistance in ferromagnetic insulator/normal metal hybrids, Phys. Rev. B **87**, 224401 (2013).

[26] Y. Chen, S. Takahashi, H. Nakayama, M. Althammer, S. T. B. Goennenwein, E. Saitoh, and G. E. W. Bauer, Theory of spin Hall magnetoresistance, Phys. Rev. B **87**, 144411 (2013).

[27] N. Vlietstra, J. Shan, V. Castel, and B. J. Van Wees, Spin-Hall magnetoresistance in platinum on yttrium iron garnet:

dependence on platinum thickness and in-plane/out-of-plane magnetization, Phys. Rev. B **87**, 184421 (2013).

[28] Z. Qiu, K. Ando, K. Uchida, Y. Kajiwara, R. Takahashi, H. Nakayama, T. An, Y. Fujikawa, and E. Saitoh, Spin mixing conductance at a well-controlled platinum/yttrium iron garnet interface, Appl. Phys. Lett. **103**, 092404 (2013).

[29] A. Aqeel, I. J. Vera-Marun, B. J. Van Wees, and T. T. M. Palstra, Surface sensitivity of the spin Seebeck effect, J. Appl. Phys. **116**, 153705 (2014).

[30] D. Kikuchi, M. Ishida, K. Uchida, Z. Qiu, T. Murakami, and E. Saitoh, Enhancement of spin-Seebeck effect by inserting ultra-thin $Fe_{70}Cu_{30}$ interlayer, Appl. Phys. Lett. **106**, 082401 (2015).

[31] X. Jia, K. Liu, K. Xia, and G. E. W. Bauer, Spin transfer torque on magnetic insulators, Europhys. Lett. **96**, 17005 (2011).

[32] H. Yuasa, K. Tamae, and N. Onizuka, Spin mixing conductance enhancement by increasing magnetic density, AIP Adv. **7**, 055928 (2017).

[33] F. Nakata, T. Niimura, Y. Kurokawa, and H. Yuasa, Spin Seebeck voltage enhancement by Mn system metals insertion at the interface between YIG and nonmagnetic layer, Jpn. J. Appl. Phys. **58**, SBBI04 (2019).

[34] A. Berger and M. R. Pufall, Generalized magneto-optical ellipsometry, Appl. Phys. Lett. **71**, 965 (1997).

[35] A. Berger and M. R. Pufall, Quantitative vector magnetometry using generalized magneto-optical ellipsometry, J. Appl. Phys. **85**, 4583 (1999).

[36] J. A. Arregi, J. B. Gonzalez-Diaz, E. Bergaretxe, O. Idigoras, T. Unsal, and A. Berger, Study of generalized magneto-optical ellipsometry measurement reliability, J. Appl. Phys. **111**, 103912 (2012).

[37] J. A. Arregi, J. B. González-Díaz, O. Idigoras, and A. Berger, Strain-induced magneto-optical anisotropy in epitaxial hcp Co films, Phys. Rev. B **92**, 184405 (2015).

[38] P. Riego, S. Tomita, K. Murakami, T. Kodama, N. Hosoito, H. Yanagi, and A. Berger, Enhanced magneto-optical Kerr effects in Py/Ag/Bi trilayers, J. Phys. D: Appl. Phys. **50**, 19LT01 (2017).

[39] W. Lin, K. Chen, S. Zhang, and C. L. Chien, Enhancement of Thermally Injected Spin Current through an Antiferromagnetic Insulator, Phys. Rev. Lett. **116**, 186601 (2016).

[40] M. A. Musa, R. S. Azis, N. H. Osman, J. Hassan, and T. Zangina, Structural and magnetic properties of yttrium iron garnet (YIG) and yttrium aluminum iron garnet (YAlG) nanoferrite via sol-gel synthesis, Results Phys. **7**, 1135 (2017).

[41] See Supplemental Material at http://link.aps.org/supplemental/10.1103/PhysRevB.102.094411 for thermoelectric voltage and magnetoresistance dependences on magnetic fields for samples with various thickness and various insertion layers.

[42] H. L. Wang, C. H. Du, Y. Pu, R. Adur, P. C. Hammel, and F. Y. Yang, Scaling of Spin Hall Angle in 3d, 4d, and 5d Metals from $Y_3Fe_5O_{12}$/Metal Spin Pumping, Phys. Rev. Lett. **112**, 197201 (2014).

[43] J. X. Li, M. W. Jia, Z. Ding, J. H. Liang, Y. M. Luo, and Y. Z. Wu, Pt-enhanced anisotropic magnetoresistance in Pt/Fe bilayers, Phys. Rev. B **90**, 214415 (2014).

[44] J. C. Slater, The ferromagnetism of nickel. II. Temperature effects, Phys. Rev. **49**, 931 (1936).

[45] L. Pauling, The nature of the interatomic forces in metals, Phys. Rev. **54**, 899 (1938).

[46] M. Stampanoni, A. Vaterlaus, M. Aeschlimann, and F. Meier, Magnetism of Epitaxial bcc Iron on Ag(001) Observed by Spin-Polarized Photoemission, Phys. Rev. Lett. **59**, 2483 (1987).

[47] C. M. Schneider, P. Bressler, P. Schuster, J. Kirschner, J. J. de Miguel, and R. Miranda, Curie Temperature of Ultrathin Films of fcc-Cobalt Epitaxially Grown on Atomically Flat Cu (100) Surfaces, Phys. Rev. Lett. **64**, 1059 (1990).

[48] P. J. Jensen, H. Dreyss, and K. H. Bennemann, Thickness dependence of the magnetization and the Curie temperature of ferromagnetic thin films, Surf. Sci. **269-270**, 627 (1992).

[49] M. F. Collins, A measurement by neutron scattering of magnetic moments in a paramagnetic iron-nickel alloy, Proc. Phys. Soc. **86**, 973 (1965).

[50] E. Fawcett, Spin-density-wave antiferromagnetism in chromium, Rev. Mod. Phys. **60**, 209 (1988).

[51] S. M. Wu, J. E. Pearson, and A. Bhattacharya, Paramagnetic Spin Seebeck Effect, Phys Rev. Lett. **114**, 186602 (2015).

[52] T. Moriya and A. Kawabata, Effect of spin fluctuations on itinerant electron ferromagnetism. II, J. Phys. Soc. Jpn. **35**, 669 (1973).

[53] T. Moriya, *Spin Fluctuations in Itinerant Electron Magnetism* (Springer, Berlin, 1985).

[54] Y. Ohnuma, H. Adachi, E. Saitoh, and S. Maekawa, Enhanced dc spin pumping into a fluctuating ferromagnet near T_c, Phys. Rev. B **89**, 174417 (2014).

[55] B. Khodadadi, J. B. Mohammadi, C. Mewes, T. Mewes, M. Manno, C. Leighton, and C. W. Miller, Enhanced spin pumping near a magnetic ordering transition, Phys. Rev. B **96**, 054436 (2017).